Quantitative Detection of Cell Activity by Measuring the Fluctuation of Intracellular Motility

Morito Sakuma[#], Yuichi Kondo and Hideo Higuchi[*]

Department of Physics, Graduate School of Science, The University of Tokyo, 7-3-1 Hongo Bunkyo-ku, Tokyo 113-0033, Japan.

*Correspondence: higuchi@phys.s.u-tokyo.ac.jp (H.H.)

[#] **Present address:** Michael Smith Laboratories, The University of British Columbia, 2185 East Mall, Vancouver, BC, V6T 1Z4, Canada

Abstract

The measurement of cell activity changes during damage is important to understand the process of cell death and evaluate the effect of medicines. To evaluate cell activity generally, we extended the method of intensity fluctuation in which intensity change in the pixel induced by the movement of organelles was calculated. Cancer, endothelial and iPS cells were damaged by reactive oxygen species (ROS) generated by a fluorescent dye (IR700), hydrogen peroxide, and ultraviolet light. The intensity fluctuation in damaged cells gradually decreased independent of the kind of cell, indicating that the decrease in the fluctuation is a general phenomenon in damaged cells. The rupture of vesicles and mitochondria in the cells were observed upon ROS production. The motility of purified kinesin and dynein which transport vesicles and organelles was inhibited by ROS. These suggest that ROS and cytotoxic molecules spreading from ruptured organelles contribute to the reduction in cell activity which brings about the decrease in the motility and intensity fluctuation of organelles driven by kinesin and dynein.

Introduction

The intracellular condition of cells is changed by external stresses, such as oxidation, no physiological pH and toxins. The accumulation of those stresses leads to cell death (Fujii et al., 2003; Lagadic-Gossmann et al., 2004; Martindale and Holbrook, 2002; Redza-Dutordoir and Averill-Bates, 2016). In the process of cell death, the accumulated damage exceeds a certain threshold, and then the cells switch on the systems for cell death, called apoptosis, or develop coagulative and liquefactive necrosis (Gascoigne and Taylor, 2009; Letai, 2015). These processes are common in various types of cells, including pluripotent stem cells and cancer cells. Therefore, detecting the accumulation of damage is important to evaluate the effect or tolerance of medicines on cells and their culture environment.

Fluorescent probes have been used to detect changes in intracellular conditions during cell death by specifically staining proteins related to cell death (Bussolati et al., 2011; Shi et al., 2012; Yamaguchi et al., 2011; Zhang et al., 1997; Zhang et al., 2015). However, fluorescence probes have problems such as photobleaching and phototoxicity. The accuracy of the detection of cell damage decreases with the decrease in intensity of fluorescent probes induced by photobleaching (Gerlich and Ellenberg, 2003; Laissue et al., 2017; Waters, 2009). Therefore, fluorescent probes for detecting sequential changes in the activity longer than ~10 minutes are not available. Conventional microscopes such as bright field, phase contrast and differential interference contrast microscopes have been used to detect cell activity and damage for a long time because they cause essentially no photobleaching or photodamage (Aftab et al., 2014; Ma et al., 2019; Maddah et al., 2015). In these works, cell activity was usually detected by the morphological and motility changes of whole cells. However, since the morphological changes of cells caused by mild cell damage were not detected and the motility of the cell was stochastic and random, these methods were not precise and quantitative (Aftab et al., 2014; Balvan et al., 2015; Tokumitsu et al., 2010). Therefore, to detect precise and quantitative changes caused by damage over a long time, specific and precise changes in damaged cells should be detected under a conventional microscope.

In previous work, the reduction in the motility of intracellular organelles was detected without morphological changes of cells under a phase contrast microscope (Sakuma et al., 2016). This is supported by the result that the motility of mitochondria was suppressed by cell damage (Debattisti et al., 2017;

65   Liao et al., 2017). The motility of mitochondria gradually decreased just after the
66   addition of hydrogen peroxide, and the decrease in the motility reached 50%
67   within 10 minutes (Debattisti et al., 2017). These results suggested that the
68   effect on the motility of organelles in damaged cells occurred earlier than the
69   changes in cell morphology and motility. Thus, the method of detecting
70   intracellular motility under a conventional microscope would overcome the
71   disadvantages of previous fluorescence, morphological, and cell motility
72   methods. However, little is understood about the generality and mechanism of
73   motility reduction.

74   In this study, various cells were damaged by several methods, including
75   photoactivation of IR700, irradiation with ultraviolet (UV) light and treatment with
76   hydrogen peroxide (H_2O_2), and the change in the motility of organelles was
77   quantitatively evaluated by the developed intensity fluctuation method (IFM). We
78   found that all cells showed a decrease in motility caused by damage. To
79   elucidate the mechanisms of the decrease in motility in damaged cells, we
80   measured the reduction in the motile speeds of single vesicles in cells and in
81   purified kinesin and dynein *in vitro* assays. These measurements revealed that
82   the decrease detected by IMF resulted in the reduction in the organelle motility
83   driven by motor proteins. Since the transport system commonly exists in animal
84   cells, the decrease in the motility or transport of organelles would be a universal
85   phenomenon in various kinds of cells.

Results

1 Decrement of motility of organelles in damaged cells

Changes in the motility of organelles in damaged cells were evaluated by the intensity fluctuation method (IFM) in various cell types. Six kinds of cells, four cancer cell lines, one endothelial cell line, and one iPS cell line, were damaged by the photoactivation of IR700 dye, which is applied for the targeted therapy of cancer cells (Mitsunaga et al., 2011). IR700-EGFP was endocytosed, and the fluorescence of IR700 excited by a red laser was observed inside cells, especially near the nucleus (first and second columns in Fig. 1a). We applied the IFM to detect changes in organelle motility. The changes in intensity fluctuation were shown by heat maps of fluctuation values (third and fourth columns in Fig. 1a). All cells showed a decrease in the fluctuation values induced by photoactivation for one and ten seconds. The mean intensity fluctuation (see Materials and methods) for each kind of cell was calculated (Fig. 1b). The fluctuation values of cells that were illuminated by a red laser without adding IR700 showed no significant changes (left column in Fig. 1b). The fluctuation values in the cancer cells and HUVECs were decreased by ~30% and ~50% at 1 and 10 seconds of photoactivation, respectively, and the corresponding values in iPS cells were decreased by ~15% and ~22% (second and third columns in Fig. 1b). The fluorescence intensity of IR700 in iPS cells was ~10 times lower than that in other cells, indicating that the concentration of IR700 endocytosed in iPS cells was lower than that endocytosed in cancer cells, consistent with the lower decrease in the fluctuation value. In contrast to the significant fluctuation change, the shapes of the cells at 1 minute after 10 seconds photoactivation were not changed (Supplemental Fig. 1c). These results indicated that damage would significantly reduce the motility of organelles without causing significant changes in cell shape.

114
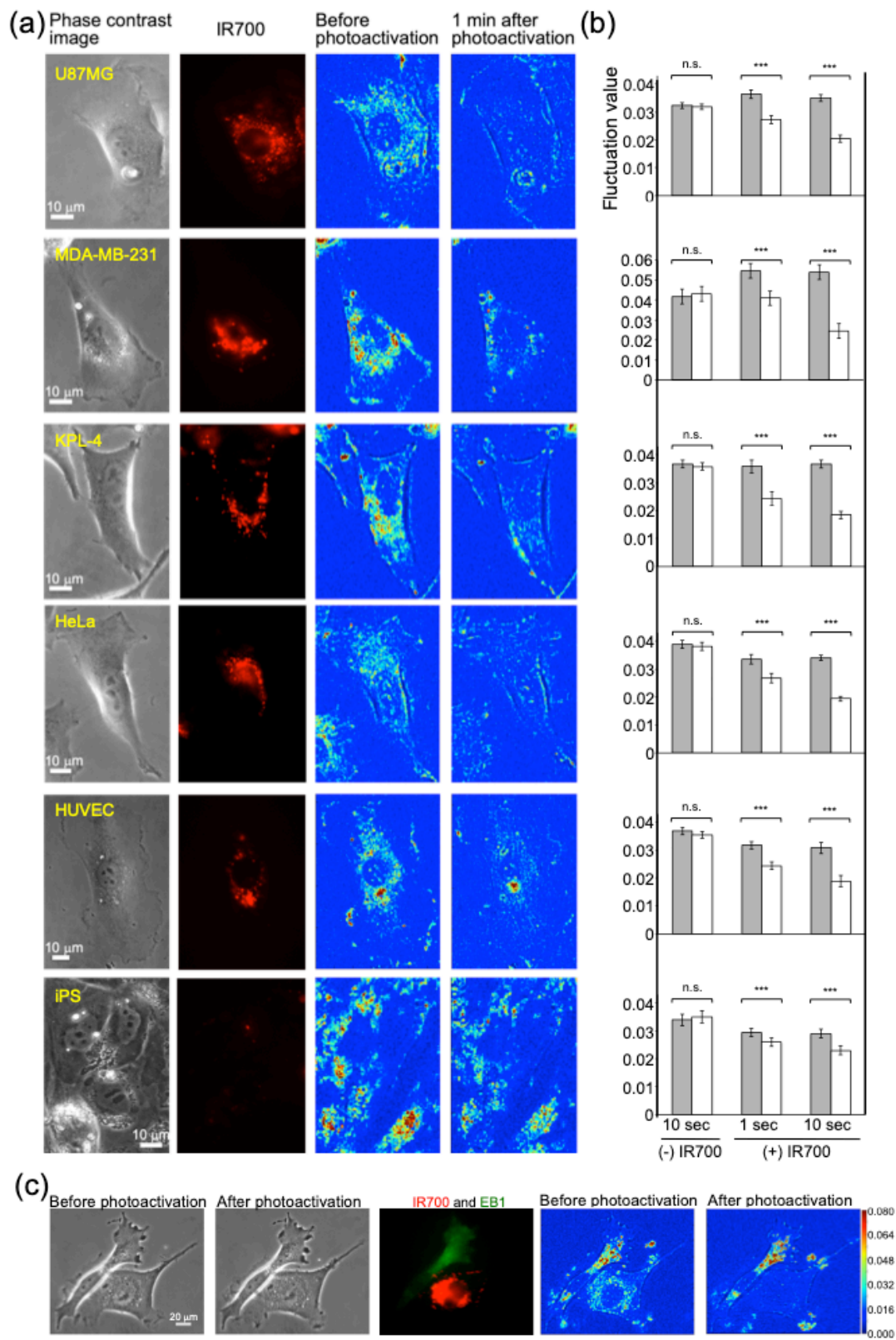
115

116 **Figure 1.** Decreased motility of organelles induced by photoactivation of IR700

117 in various cell lines. (a) Typical images of the change in motility caused by 10

118 seconds of photoactivation of IR700 in U87MG, MDA-MB-231, KPL-4, HeLa,

119 HUVEC, and iPS cells. The first column shows phase contrast images before

120 cell damage, and the second column shows the fluorescence of IR700

121 corresponding to the phase contrast images. The third and fourth columns show

122 heat maps of the change in fluctuation values through photoactivation of IR700

123 corresponding to the phase contrast images. The scale of the heat maps is the

124 same as that in Fig. 1c. (b) Change in the mean of the fluctuation values with or

125 without IR700 (mean ± SEM) (n.s. denotes not significant, ***$p<0.05$). IR700 was

126 activated for 1 or 10 seconds. (c) Detection of cell damage in co-cultured

127 U87MG and GFP-EB1-expressing MDA-MB-231 cells. The first and second

128 columns show phase contrast images before and after 10 seconds of

129 photoactivation of IR700. The third column shows the fluorescence of IR700 in

130 U87MG cells and GFP-EB1 in MDA-MB-231 cells. The fourth and fifth columns

131 show heat maps of the change in fluctuation value induced by IR700

132 photoactivation.

133

134   U87MG cells containing IR700 and MDA-MB-231-GFP-EB1 cells without
135 IR700 were cocultured and were illuminated with a red laser (Fig. 1c).
136 Fluorescence images showed that the left and right cells in Fig. 1c were
137 MDA-MB-231 and U87MG cells, respectively (third column in Fig. 1c). Phase
138 contrast images were observed before and at 2 minutes after 10 seconds of
139 photoactivation (first and second columns in Fig. 1c). While the change in cell
140 shape caused by photoactivation could hardly be distinguished in the phase
141 contrast images, the decrease in motility in only U87MG cells after
142 photoactivation was clearly observed. These results indicate that the IFM
143 selectively detected the damaged cells.

144   Cell damage was also measured by ethidium homodimer-1 (EthD-1),
145 which is one of the conventional methods for detecting cell damage. After 1
146 second of photoactivation, the nuclei of cells were not stained significantly by
147 EthD-1 (Supplemental Fig. 2). The nucleus was stained at 1 hour but not 30
148 minutes after photoactivation, suggesting that the IFM detected cell damage
149 more rapidly than staining with EthD-1.

150

151 **2 Motility changes of organelles in oxidative stress**

152   To evaluate whether the decrease in motility could become an indicator
153 of cell damage, cells were damaged by hydrogen peroxide (H_2O_2) treatment and
154 ultraviolet (UV) light irradiation. H_2O_2 was added to the culture medium at a final
155 concentration of 100 μM, and phase contrast images of cells were observed for
156 4 hours (Fig. 2a). In the phase contrast images, apparent changes in size and
157 shape could hardly be observed within 60 minutes. At 240 minutes, needle-like
158 structures were observed near the edge of cells that maintained their
159 desmosomes. The cell area gradually decreased until 240 minutes (slope: -0.05
160 (% area/minutes); blue triangles in Fig. 2b). The fluctuation value decreased
161 exponentially with the time over 10 minutes (red circles in Fig. 2)). A decrease in
162 the fluctuation was also observed after UV irradiation without a significant
163 change in cell area (Supplemental Fig. 3). These results indicated that the
164 intensity fluctuation was decreased by oxidative stress and that the decrease in
165 the intensity fluctuation was more rapid than the changes in the cell area.
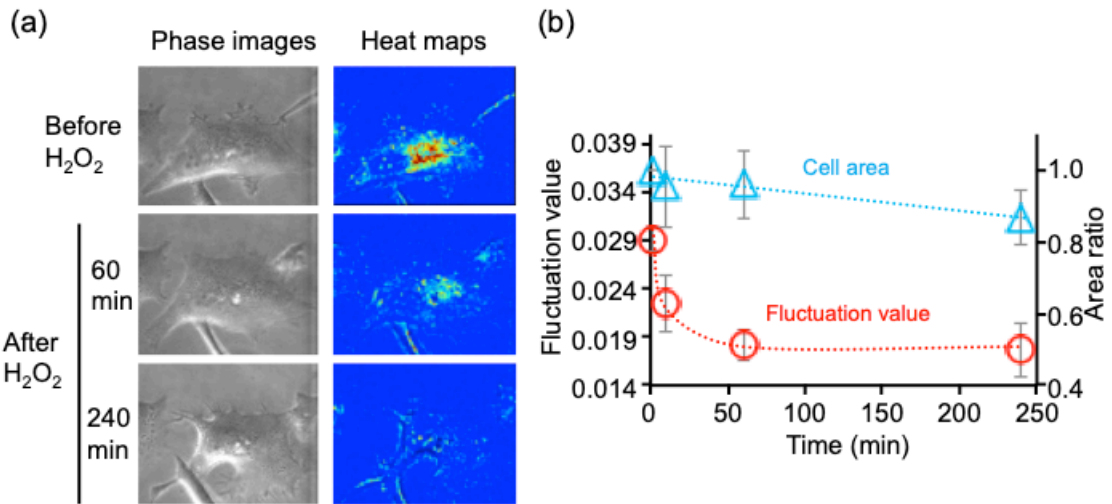
Figure 2. Decreased motility of organelles induced by the addition of hydrogen peroxide (H_2O_2). (a) Typical phase contrast images of cell and heat maps of fluctuation values corresponding to the phase contrast images before and after the addition of H_2O_2. (b) Change in fluctuation value (red circles) and cell area (light blue triangles) caused by the addition of H_2O_2 (mean ± SEM). The first and second y-axes denote the mean fluctuation values and area ratios, respectively. Broken lines show exponentially fitted lines.

174

175

3 Ruptures of vesicle and mitochondria by photoactivation of IR700

To understand the reason for the reduction in the motility of organelles, the changes in the intercellular organelles in damaged cells were measured. At 1 hour after adding IR700, most of the IR700 fluorophores were observed near the nucleus (Fig. 3a). The fluorescence intensity of those vesicles gradually decreased upon irradiation with the red laser because of photobleaching and then decreased rapidly at 3-4 seconds (Fig. 3a and b). Diffusion of IR700 fluorescence from the large vesicles to the cytoplasm was also observed (Supplemental Fig. 4), indicating that vesicles containing IR700 became ruptured or leaky and that IR700 and toxic molecules, such as protease and reactive oxygen species, would diffuse in the cytosol.

Mitochondria are one of the organelles that could be observed by a phase contrast microscope. Next, mitochondria were stained with CellROX, which is an indicator of reactive oxygen species (ROS), to observe their movement following cell damage. Mitochondria generate ROS and thus can be stained by CellROX (left and upper panels in Fig. 3c). Under photoactivation, the tubule-like structure of the mitochondria rapidly disappeared, and the fluorescence of IR700 did not accumulate in the mitochondria (right and lower panel in Fig. 3c). At the same time, the fluorescence intensity in the cytoplasm was increased, indicating that ROS in the mitochondria diffused into the cytoplasm by mitochondrial rupture, thereby enhancing the fluorescence intensity of CellROX in the cytoplasm (right and lower panels in Fig. 3c). These results suggested that vesicles and mitochondria were damaged by the photoactivation of IR700, and toxic molecules, including proteases and ROS, diffused from ruptured organelles to the cytoplasm.
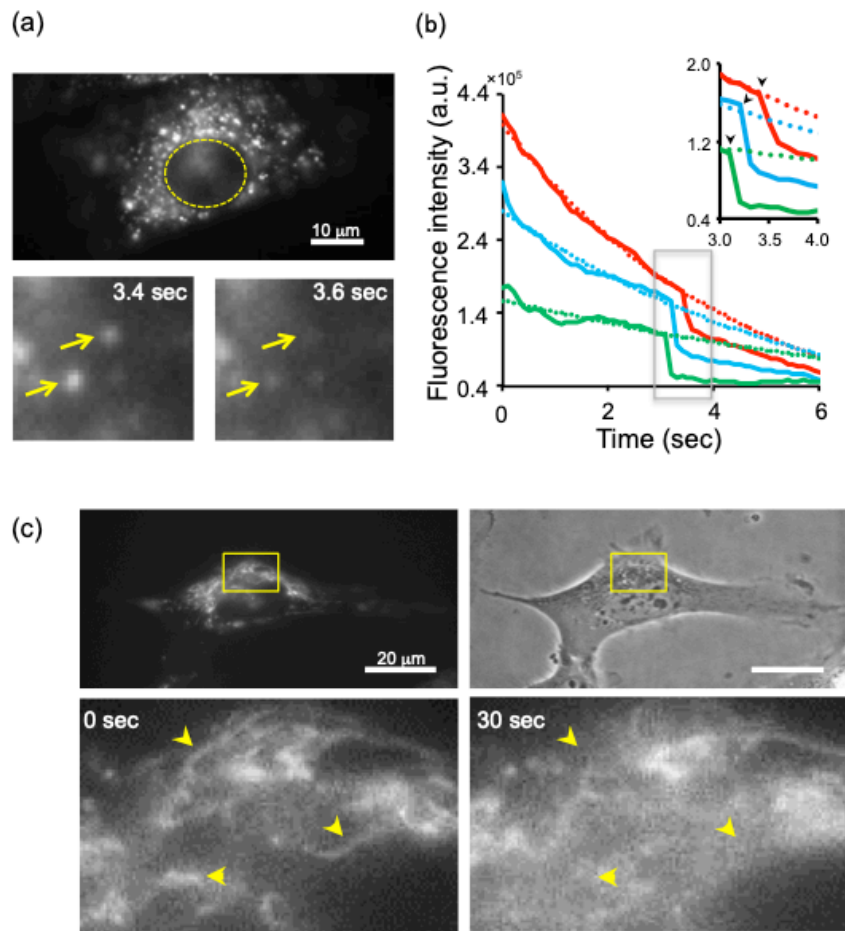
Figure 3. Real-time imaging of damage to organelles induced by the photoactivation of IR700. (a) Real-time imaging of IR700 fluorescence in vesicles. The upper image shows the distribution of the fluorescence of IR700. The yellow broken line shows the periphery of the nucleus. The lower images show the rapid decrease in IR700 fluorescence in vesicles (yellow arrows). (b) Trajectories of the fluorescence intensity of IR700. Solid and broken lines show the change in measured fluorescence intensity and exponentially fitted lines within 2.5 seconds, respectively. Black arrows in the inset image show the rapid decrease in the intensity caused by IR700 photoactivation. (c) Dynamics of mitochondria upon photoactivation of IR700. Upper images show mitochondria stained by the fluorescent probe CellROX (left) and the corresponding phase contrast image (right). Lower images show changes in the distribution of mitochondria upon photoactivation for 30 seconds. Lower images are the magnified views of the areas in the white rectangles in the upper images. Yellow arrows indicate that the rod-shaped structure of mitochondria disappeared upon photoactivation of IR700.

11

4 Motility of vesicles in damaged cells detected by quantum dots

In phase contrast microscopy, various shapes and sizes of organelles were observed. The IFM mainly detected changes in the motility of organelles near the nucleus, where endosomes and lysosomes are mainly located. Thus, the change in those organelles was directly observed and evaluated by single-particle tracking of QD-EGFR conjugates. QD-EGFR was endocytosed in vesicles and transported near the nucleus (Fig. 4a). Before damaging the cell, the vesicle-QDs moved linearly and randomly (blue line in the inset image of Fig. 4b). The linear region is presumably transported by molecular motors such as kinesin and dynein. After cell damage, the motility of the vesicles was decreased, and the trajectories of the vesicles-QDs showed confined movement (red line in the inset image). The mean-square displacements (MSDs) were also decreased by cell damage. The diffusion coefficients before and after damage were obtained by fitting the MSD plot with the equation $4Dt$, where D and t are the diffusion coefficient and time, respectively. The diffusion coefficients obtained before and after the damage were 0.42 μm^2/s and 0.07 μm^2/s, respectively. These results indicated that the diffusion after damage was approximately 6 times lower than that before damage.

The timing of the decrease in vesicle QDs was evaluated in damaged cells and compared with the results of the IFM. The fluctuation of the position of the vesicles-QDs was measured instead of the intensity fluctuation since the fluorescence intensity of QDs gradually changed upon excitation with a green laser and photoactivation of IR700 and since the fluctuation of QDs could hardly be precisely evaluated (Supplemental Fig. 5) (Li et al., 2006). The fluctuation of position was calculated from the mean standard deviations of the displacement of vesicles-QDs at every 10 frames (Fig. 4c). The fluctuation of position gradually decreased after photoactivation of IR700. The time-course change of the intensity fluctuation under a phase contrast microscope was also measured, and the decrease was compared between vesicles-QDs and IFM (Fig. 4d). The intensity fluctuation of organelles gradually decreased in parallel with the decrease in the fluctuation of the position of the vesicles-QDs, suggesting that this change in the motility of endosomes and lysosomes was coupled with the change in the motility of organelles detected by the IFM.

252
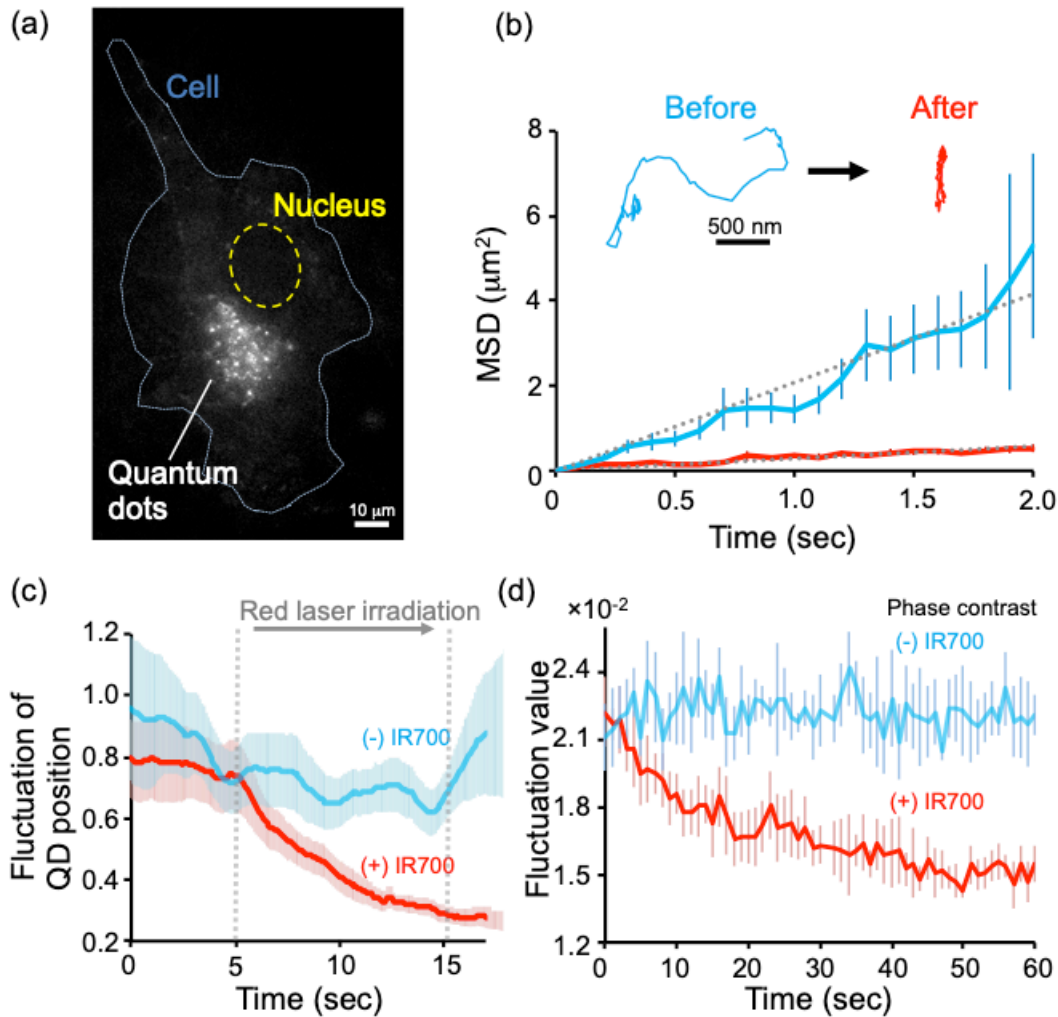
Figure 4. Single-particle tracking of vesicles labeled with quantum dots (vesicle-QDs) in damaged cells. (a) Distribution of vesicle-QDs inside cells. Blue and yellow broken lines show the periphery of the cell and nucleus, respectively. (b) Mean-square displacement (MSD) plot of the motility of vesicle-QDs before and after IR700 photoactivation (mean ± SEM). Light blue and red solid lines show the MSD before and after photoactivation, respectively. Inset image shows a typical trajectory of vesicle-QDs. Broken gray lines show lines linearly fit to the MSD values. (c) Fluctuation of the position of vesicle-QDs upon photoactivation with or without using IR700 (mean ± SEM). The cells were irradiated with a red laser from 5 to 15 seconds (gray broken line). (d) Real-time change in fluctuation values calculated from phase contrast images with or without using IR700 (mean ± SEM). The cells were irradiated with a red laser from 2 to 32 seconds.

13

265

266

5 Decrease in motilities of kinesin and dynein by oxidative stress

Vesicles including endosomes and lysosomes are transported by molecular motors, such as kinesin and dynein, along with microtubules. Therefore, the effects of IR700 photoactivation and hydrogen peroxide (H_2O_2) treatment on motor proteins were evaluated by an *in vitro* motility assay (Fig. 5a) (Higuchi et al., 2002). Bovine serum albumin (BSA) conjugated with IR700 and biotin were bound to the surface of a glass chamber. Biotinized kinesin or dynein was attached to BSA-biotin via streptavidin, and then microtubules were flowed into the chamber (Fig. 5a). The microtubules were distributed homogeneously before photoactivation (left column in Fig. 5c). After photoactivation, the microtubules accumulated within the area of photoactivation as a result of slow movement, while the motility outside the area was hardly changed (right column in Fig. 5c). The position of the leading edge of the microtubules was tracked every 10 seconds to understand the velocity change in response to oxidative stress (Fig. 5b and d). Microtubules driven by kinesin and dynein moved linearly and continuously before damage, while the motility decreased very much inside the red circles (Fig. 5d). The velocity after the photoactivation of IR700 and addition of H_2O_2 was analyzed from the trajectories of microtubules inside the photoactivated area (Fig. 5b). After photoactivation, the mean velocity of the microtubules driven by kinesin and dynein was decreased from 394 to 6 nm/s and from 99 to 4 nm/s, respectively. The velocity also decreased from 467 to 48 nm/s at 60 minutes in the presence of 0.1 mM H_2O_2. It is noted that the motility of kinesin was not inhibited by red laser irradiation without using IR700 (Supplemental Fig. 6a). The addition of an ROS scavenging system (GCOβ) also prevented the decrease in the motility of kinesin caused by the photoactivation of IR700 (Supplemental Fig. 6b). These results indicate that the decrease in the motility of kinesin and dynein was induced by oxidative stress.
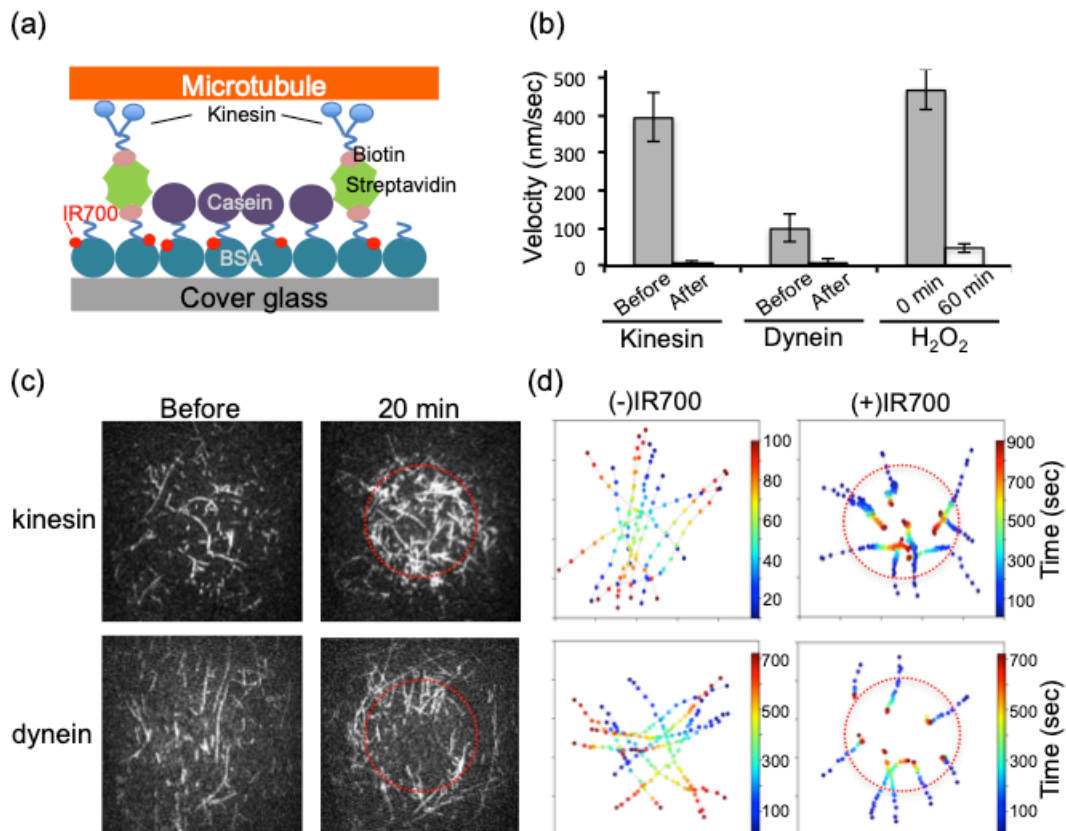
Figure 5. Motility assay of kinesin and dynein on microtubules under oxidative stress. (a) Schematic illustration of the motility assay. Microtubules were fixed on the cover glass by binding with kinesin or dynein. IR700 binds to BSA through the NHS moiety. Photoactivation of IR700 damages molecular motors and microtubules. (b) Decreased motility of kinesin and dynein upon photoactivation of IR700 and addition of hydrogen peroxide (H_2O_2). Gray and white bars indicate the velocity before and after photoactivation and addition of H_2O_2 (mean ± SEM), respectively. The red laser was irradiated for 100 milliseconds, and the final concentration of H_2O_2 was 100 μM. (c) Change in the distribution of microtubules caused by photoactivation. The red laser was irradiated during the period inside the red broken lines, and the fluorescence of the microtubules was observed for 20 minutes. (d) Trajectories of microtubules before and after photoactivation. Color bars indicate observation time, and red broken lines denote the spots irradiated with the red laser corresponding to (c).

15

Discussion

Advantage of the intensity fluctuation method (IFM) in detecting cell damage

The motility of organelles in several cell lines, including cancer cells, endothelial cells and iPS cells, was detected by the intensity fluctuation method (IFM) (Fig. 1a). The sensitivity and quantitativity of measurements of the fluorescence probes decrease by the photobleaching, phototoxicity and background of the free probes (Laissues et al., 2017; Waters 2009). Actually, a background of EthH-1 in the cytoplasm and nucleus was high even in intact cells, and the fluorescence intensity in the nucleus showed diversity among each cell (Supplemental Fig. 2). The IMF detected damage of cells even when EthH-1 staining did not detected the damage (Sakuma et al. 2016).

Observation of cell morphology and motility under label-free microscopes such as phase contrast is not so quantitative because of polymorphism of cell (Ebara et al., 2018; Li et al, 2006; Masuzzo et al., 2016). In this study, the damage of cell was detected by IFM even when the changes in the areas and shapes of the cell were not detected (Fig. 2 and Supplemental Fig. 1c). These indicate that the IFM is more sensitive and quantitative than the fluorescence, motility and morphology methods (Fig. 1, 2, and 4).

Oxidative stresses induced the decrement of the motility of organelles

Intensity fluctuation that indicates the motility of organelles was gradually decreased upon IR700 photoactivation, H_2O_2 treatment, and UV irradiation. What material generated from these methods suppressed the motility of organelles? Photoactivation of IR700 was recently developed to specifically damage cancer cells *in vitro* and *in vivo* (Harada et al., 2015; Nagaya et al., 2016). Previous research has shown that photoactivation induces cellular damage by producing ROS and heat (Mitsunaga et al., 2011; Kishimoto et al., 2015). To specify the effect of photoactivation, we applied a motility assay of kinesin and dynein to microtubules (Fig. 5). The motility of microtubules inside the photoactivated region rapidly decreased (Fig. 5b-d). However, the motility of kinesin in the presence of oxygen scavenging reagents that removed ROS was almost constant upon IR700 photoactivation (Aitken et al., 2008; Harada et al., 1990) (Supporting Fig. 6b). Therefore, our results indicated that the production of ROS induced by the photoactivation of IR700 is a main factor in inhibiting the motility of motor proteins. H_2O_2 is one form of ROS and indiscriminately induces

16

346 oxidation stress toward protein, lipids, mitochondria, and DNA (Redza-Dutordoir
347 and Averill-Bates, 2016). UV irradiation also produces ROS from cytoplasmic
348 molecules and damages proteins and DNA (Heck et al., 2003). Therefore, all
349 methods produced ROS for damaging cells, and the decrease in the motility of
350 organelles driven by motor proteins would be an indicator of cell damage
351 induced by ROS.
352
353 **Universality of the decrease in the motility of organelles in damaged cells**
354 The intensity fluctuation detected the movement of organelles including
355 vesicles, mitochondria, Golgi and endoplasmic reticulum. Most animal cells
356 showed the dynamics of those organelles, and thus, our IFM could easily be
357 applied to detect damage in various types of cells.
358 We showed the inhibition of organelle transportation at high levels of
359 ROS. This result is consistent with the finding that an elevated level of ROS
360 induced by mitochondrial and lysosomal damage is observed during apoptosis in
361 many cell types (Murphy MP, 2013; Redza-Dutordoir and Averill-Bates, 2016).
362 Not only ROS but also acid and protease leaked from the damaged mitochondria
363 and lysosomes would inhibit organelle transportation (Boya and Kroemer, 2008).
364 Acidification of the cytoplasm is also observed in the process of apoptosis and
365 with increases in ROS (Clément et al., 1998; Lagadic-Gossmann et al., 2004,
366 Sakuma et al., 2016). The bacterial cytoplasm showed decreased diffusion at
367 lower cytoplasmic pH (Maharana et al., 2016), and thus, the change in physical
368 properties of the cytoplasm would correlate with the decrease in the motility of
369 organelles. Therefore, a decrease in organelle motility is generally observed in
370 various types of cell damage and cell death.

Conclusion

Our novel intensity fluctuation method (IFM) analyzing phase contrast images quantitatively detected cell damage. The reduction in the motility of organelles in damaged cells was successfully measured by the decrease in intensity fluctuation. Vesicle transport in damaged cells and the motility of purified motor proteins were inhibited by cell damage, indicating that a reduction in the motility of motor proteins and organelle transport would induce a decrease in the intensity fluctuation. The reduction in the motility of organelles was also observed upon oxidative stress induced by ultraviolet light irradiation and H_2O_2 treatment. Reactive oxygen species would be produced in the process of cell death, and thus, the decrease in motility would be commonly observed in damaged cells. Therefore, our IFM would be applicable to the facile and quantitative detection of several kind of cell damage or cell death.

Materials and method

Cell culture and preparation

Glioblastoma cells (U87MG, American Type Culture Collection, Manassas, Virginia), breast cancer cells (KPL-4, Kawasaki Medical School) (Tada et al., 2007), and cervical cancer cells (HeLa, Cell Resource Center for Biomedical Research·Cell Bank at Tohoku University) were cultured at 37 ℃ with 5% CO_2 and 95% air in Dulbecco's modified Eagle's medium (DMEM, Sigma-Aldrich, St. Louis, Missouri) supplemented with 10% fetal bovine serum (FBS, Takara Bio Inc., Shiga, Japan), 1% L-glutamine (Nacalai Tesque, Kyoto, Japan), and 100 U/mL penicillin-streptomycin (Wako Pure Chemicals Industries, Osaka, Japan). Wild-type MDA-MB-231 (Summit Pharmaceuticals International) and GFP-EB1 (end binding protein-1)-expressing MDA-MB-231 cells were cultured at 37 ℃ without CO_2 in Leibowitz's L-15 medium (L-15, ThermoFisher Science, Waltham, Massachusetts) supplemented with 10% FBS, 1% L-glutamine, and 100 U/mL penicillin-streptomycin. Human umbilical vein endothelial cells (HUVECs, Thermo Fisher Science) were cultured at 37 ℃ with 5% CO_2 and 95% air in Medium 200 (Thermo Fisher Science) supplemented with 50× low serum growth supplement (LSGS, Thermo Fisher Science) and 100 U/mL penicillin-streptomycin. Human induced pluripotent stem cells (iPS, The Institute of Medical Science, The University of Tokyo) were cultured at 37 ℃ with 5% CO_2 and 95% air in ReproFF (ReproCELL, Kanagawa, Japan) supplemented with 5 ng/mL basic fibroblast growth factor (bFGF, PeproTech Inc., Rocky Hill, New Jersey). U87MG, KLP-4, HeLa, MDA-MB-231, and HUVECs were confluently cultured on polystyrene cell culture dishes and recovered by using 1× TrypLE express enzyme (Thermo Fisher Science). The concentration of recovered cells was adjusted to 1.0×10^4 cells/mL, and the suspension was seeded on a glass-bottom dish (Matsunami Glass Ind., Ltd., Gunma, Japan) coated with 2% collagen. iPS cells were cultured on cell culture dishes coated with a Matrigel (Corning, Tewksbury, Massachusetts) and formed colonies. After the size of the colonies reached approximately 1 mm, the cells were treated with dissociation solution for human ES/iPS cells (ReproCELL) and recovered by using a cell scraper. The colonies were broken up to approximately 200 μm by gentle pipetting and seeded on a glass-bottom dish coated with Matrigel. After being cultured for one day at 37 ℃, all cells were prepared for the following experiments.

19

Fluorescence staining of cells

Mitochondria in cells were stained by CellROXorange (Thermo Fisher Science). The final concentration of CellROX was 5 μM, and the fluorescence of CellROX was observed after incubating for 10 minutes at 37 ℃ and washing. Quantum dots (QD605) were used to observe the movement of vesicles in cells. QD605 was conjugated with an antibody against epithelial growth factor receptor antibody (Abcam, Cambridge, United Kingdom) (QD-EGFR) by using an antibody conjugation kit (Qdot™ 605 Antibody Conjugation Kit, Thermo Fisher Science). QD-EGFR was added to the culture medium of cells at a final concentration of 5 nM, and the cells were incubated for 10 minutes at 37 ℃. After washing three times with culture medium and incubating for 1 hour at 37°C, the fluorescence of endocytosed QD-EGFR was observed. Cell damage was evaluated by ethidium homodimer-1 (EthD-1). EthD-1 was added at a final concentration of 5 μM after damaging cells.

Damaging cells

Cells were damaged by the photoactivation of IR700, addition of hydrogen peroxide (H_2O_2), and irradiation with ultraviolet (UV) light. IRDye 700DX NHS ester (IR700, Li-COR Bioscience, Lincoln, Nebraska) and anti-EGFR antibody (Abcam) were conjugated for 2 hours at room temperature in 10 mM Na_2HPO_4 (pH 8.0) (Mitsunaga et al., 2011). The conjugates (IR700-EGFR) were added to the culture medium of cells at a final concentration of 1 μM, and the cells were incubated for 1 hour at 37 ℃ and washed two times with culture medium. To damage cells by oxidative stress, the cells were treated with hydrogen peroxide (H_2O_2, Wako Pure Chemicals). H_2O_2 was added to the culture medium of cells at a final concentration of 100 μM. After the addition of H_2O_2, the cells were continuously observed by a phase contrast microscope. Cells were damaged by ultraviolet (UV) light at a wavelength of 360-370 nm including a Hg-lamp spectrum. A fluorescence filter set (excitation filter: BP360-370, emission filter: BA420, dichromatic mirror: DM400, U-MNUA2, Olympus, Tokyo, Japan) and a mercury lamp (Olympus) were used for UV light irradiation, and the cells were irradiated with UV light for 10 seconds.

Fluorescence microscopy for observing cells and proteins

All images of cells were taken by an inverted microscope (IX-70,

20

456 Olympus) equipped with a phase contrast objective lens (PLAPON 60XOPH,
457 Olympus), halogen and mercury lamps (U-LH100 and U-ULS100HG, Olympus),
458 EMCCD cameras (iXon 3, Andor Technology Ltd., Belfast, Northern Ireland),
459 and an incubator (TOKAI HIT Co., Ltd., Shizuoka, Japan) as reported previously
460 with modifications (Sakuma et al., 2016). The temperature and concentration of
461 CO_2 were maintained at 37 ℃ and 5%, respectively, by the incubator. During
462 the acquisition of phase contrast images, halogen light was passed through a
463 510-550 nm bandpass filter to prevent photoactivation of IR700. IR700 was
464 photoactivated by using a red laser (635 nm, 100 mW, Barrington, Edmund
465 Optics, New Jersey), and the fluorescence was observed by a camera equipped
466 with a 690-730 bandpass filter. The fluorescence of QD-EGFR, CellROX,
467 rhodamine, and EthD-1 was observed with illumination by a green laser (532 nm,
468 Showa Optronics, Tokyo, Japan) and detected by a camera (EMCCD, Andor
469 iXon-plus 885) equipped with a 600-620 nm bandpass filter. GFP-EB1 was
470 observed under a blue laser (488 nm, Showa Optronics) and detected by a
471 camera equipped with a 510-550 nm bandpass filter.

472

473 **Intensity fluctuation method (IFM) to detect cell damage**

474 To detect the motility change of organelles caused by cell damage, the
475 intensity fluctuation of pixels in phase contrast images was calculated. The
476 intensity fluctuation ($\Delta I/<I>$) was calculated by the standard deviation (ΔI) of the
477 intensity divided by the mean intensity ($<I>$) of a pixel according to previous
478 methods with modification (Sakuma et al., 2016). The phase contrast images of
479 cells were taken for 300 frames at 10 (Fig. 4d) or 20 (other figures)
480 frames/second. To enhance the movement of organelles, the phase images
481 were processed by a bandpass filter with a bandwidth of 3-10 pixels (390-1300
482 nm) included in ImageJ software (Sakuma et al., 2016). Then, all phase contrast
483 images were processed with 4 × 4 binning to reduce the number of pixels in
484 order to reduce the intensity noise and save calculation time. The intensity
485 fluctuation was calculated every 10 frames (1 and 0.5 seconds). A total of 6
486 rectangles in each cell with a size of 36 (6 × 6) binned pixels were selected
487 randomly near the nucleus (Supplemental Fig. 1a). The mean intensity
488 fluctuation of 36 binned pixels was defined as one set of intensity fluctuations.
489 The p-value of fluctuation values between damaged and non-damaged cells
490 from Student's t-test was 0.07±0.04 (mean ± SE for 4 cells) at one set (10
491 frames in Supplemental Fig. 1b; p-value was out of range). To reduce the

492 p-value, the mean ± SE of multiple sets of fluctuation was calculated. The
493 p-value decreased with increasing number of sets (or frames) (green rectangles
494 in Supplemental Fig. 1b). To ensure a significant difference between the
495 damaged and non-damaged cells, we took the mean of 30 sets (or 300 frames)
496 as the intensity fluctuation. Custom code in Python was used for the calculation
497 and creation of heat maps.
498
499 **Single-particle tracking of vesicles by using quantum dots**
500   Vesicles inside cells were labeled by quantum dot-EGFR conjugates
501 (QD-EGFR). The fluorescence of vesicles was observed for 17 seconds at 10
502 frames/s including the photoactivation period (10 seconds) of IR700. The
503 localization of vesicles was estimated by fitting fluorescence-intensity profiles of
504 QDs with a two-dimensional Gaussian function (Yildiz and Selvin, 2005). From
505 the trajectories, the ensemble-averaged mean-square displacement (MSD) was
506 calculated by the following equation:

$$MSD\ (t) = \frac{1}{N}\sum_{i=1}^{N}\big((x_i(t) - x_i(0))^2 + (y_i(t) - y_i(0))^2\big)$$

507 where N is the number of particles and $x_i(t)$ and $y_i(t)$ are the coordinates of
508 particle i at time t. In total, 32 and 29 particles with and without IR700,
509 respectively, were tracked, and then the MSD was calculated on each trajectory.
510 The mean MSD from t = 0 to 2 seconds was calculated and fitted to a linear
511 equation for estimating the diffusion coefficient (D) using the equation *MSD =*
512 *4Dt* (Maharana et al., 2016).
513   The fluctuation of the localization of QDs was calculated from the
514 standard deviation of the displacement of the QDs. The standard deviation of the
515 displacement in 10 frames was calculated and then shifted by one frame in a
516 similar manner to a moving average through a total of 170 frames.
517
518 **Motility assay of kinesin and dynein**
519   A motility assay of kinesin and dynein was performed on cover glass in a
520 flow chamber (Fig. 5a). First, 1 mg/mL bovine serum albumin (BSA) conjugated
521 with biotin was flowed to cover the surface of the glass. Then, IR700 was flowed
522 to conjugate with the BSA through the NHS moiety. Next, 1 mg/mL streptavidin
523 was flowed to bind with biotin, and then 0.5 mg/mL casein was flowed to prevent
524 the nonspecific binding of kinesin and dynein to BSA or the glass surface. Dimer

525 kinesin (mouse KIF5A with 490 amino acid) or dynein (human dynein-1,
526 GST-D384) labeled with BDTC were flowed to bind with streptavidin, and tubulin
527 flowed. Purification of kinesin, dynein, and microtubules and labeling of the
528 microtubules by rhodamine were carried out according to previous reports
529 (Kinoshita et al., 2018). By adding 1 mM of ATP, the gliding of microtubules
530 labeled with rhodamine was observed by fluorescence microscopy

Acknowledgements

Competing interests

No potential conflict of interest was reported by the authors.

References

541 Aftab O, Nazir M, Fryknäs M, Hammerling U, Larsson R, Gustafsson MG. 2014.
543   Label free high throughput screening for apoptosis inducing chemicals
544   using time-lapse microscopy signal processing. *Apoptosis* **19**:1411–1418.
545   doi:10.1007/s10495-014-1009-9

546 Aitken CE, Marshall RA, Puglisi JD. 2008. An oxygen scavenging system for
547   improvement of dye stability in single-molecule fluorescence experiments.
548   *Biophys J* **94**:1826–1835. doi:10.1529/biophysj.107.117689

549 Balvan J, Krizova A, Gumulec J, Raudenska M, Sladek Z, Sedlackova M, Babula
550   P, Sztalmachova M, Kizek R, Chmelik R, Masarik M. 2015. Multimodal
551   holographic microscopy: Distinction between apoptosis and oncosis. *PLoS*
552   *One* **10**:1–16. doi:10.1371/journal.pone.0121674

553 Boya P, Kroemer G. 2008. Lysosomal membrane permeabilization in cell death.
554   *Oncogene* **27**:6434–6451. doi:10.1038/onc.2008.310

555 Bussolati O, Belletti S, Gatti R, Gazzola GC, Orlandini G, Dall'Asta V. 2011.
556   Comparison of Annexin V and Calcein-AM as Early Vital Markers of
557   Apoptosis in Adherent Cells by Confocal Laser Microscopy. *J Histochem*
558   *Cytochem* **46**:895–900. doi:10.1177/002215549804600804

559 Clément MV, Ponton A, Pervaiz S. 1998. Apoptosis induced by hydrogen
560   peroxide is mediated by decreased superoxide anion concentration and
561   reduction of intracellular milieu. *FEBS Lett* **440**:13–18.
562   doi:10.1016/S0014-5793(98)01410-0

563 Debattisti V, Gerencser AA, Saotome M, Das S, Hajnóczky G. 2017. ROS
564   Control Mitochondrial Motility through p38 and the Motor Adaptor Miro/Trak.
565   *Cell Rep* **21**:1667–1680. doi:10.1016/j.celrep.2017.10.060

566 Ebata H, Yamamoto A, Tsuji Y, Sasaki S, Moriyama K, Kuboki T, Kidoaki S.
567   2018. Persistent random deformation model of cells crawling on a gel
568   surface. *Sci Rep* **8**:1–12. doi:10.1038/s41598-018-23540-x

25

569 Fujii J, Matsui T, Heatherly DP, Schlegel KH, Lobo PI, Yutsudo T, Ciraolo GM,
570 Morris RE, Obrig T. 2003. Rapid apoptosis induced by Shiga toxin in HeLa
571 cells. *Infect Immun* **71**:2724–2735. doi:10.1128/IAI.71.5.2724-2735.2003

572 Gascoigne KE, Taylor SS. 2009. How do anti-mitotic drugs kill cancer cells? *J*
573 *Cell Sci* **122**:2579–2585. doi:10.1242/jcs.039719

574 Gerlich D, Ellenberg J. 2003. 4D imaging to assay complex dynamics in live
575 specimens. *Nat Rev Mol Cell Biol 4* **Suppl**:S14–S19. doi:10.1038/ncb1033

576 Harada T, Nakamura Y, Choyke PL, Sato K, Nagaya T, Kobayashi H. 2015.
577 Near Infrared Photoimmunotherapy Targeting EGFR Positive Triple
578 Negative Breast Cancer: Optimizing the Conjugate-Light Regimen. *PLoS*
579 *One* **10**:e0136829. doi:10.1371/journal.pone.0136829

580 Harada Y, Sakurada K, Aoki T, Thomas DD, Yanagida T. 1990.
581 Mechanochemical coupling in actomyosin energy transduction studied by in
582 vitro movement assay. *J Mol Biol* **216**:49–68.
583 doi:10.1016/S0022-2836(05)80060-9

584 Heck DE, Vetrano AM, Mariano TM, Laskin JD. 2003. UVB light stimulates
585 production of reactive oxygen species: Unexpected role for catalase. *J Biol*
586 *Chem* **278**:22432–22436. doi:10.1074/jbc.C300048200

587 Higuchi H, Muto E, Inoue Y, Yanagida T. 2002. Kinetics of force generation by
588 single kinesin molecules activated by laser photolysis of caged ATP. *Proc*
589 *Natl Acad Sci* **94**:4395–4400. doi:10.1073/pnas.94.9.4395

590 Kinoshita Y, Kambara T, Nishikawa K, Kaya M, Higuchi H. 2018. Step Sizes and
591 Rate Constants of Single-headed Cytoplasmic Dynein Measured with
592 Optical Tweezers. *Sci Rep* **8**:1–14. doi:10.1038/s41598-018-34549-7

593 Kishimoto S, Bernardo M, Saito K, Koyasu S, Mitchell JB, Choyke PL, Krishna
594 MC. 2015. Evaluation of oxygen dependence on in vitro and in vivo
595 cytotoxicity of photoimmunotherapy using IR-700-antibody conjugates. *Free*
596 *Radic Biol Med* **85**:24–32. doi:10.1016/j.freeradbiomed.2015.03.038

26

597 Lagadic-Gossmann D, Huc L, Lecureur V. 2004. Alterations of intracellular pH
598   homeostasis in apoptosis: Origins and roles. *Cell Death Differ* **11**:953–961.
599   doi:10.1038/sj.cdd.4401466

600 Laissue PP, Alghamdi RA, Tomancak P, Reynaud EG, Shroff H. 2017.
601   Assessing phototoxicity in live fluorescence imaging. *Nat Methods* **14**:657–
602   661. doi:10.1038/nmeth.4344

603 Letai A. 2015. Cell Death and Cancer Therapy: Don't Forget to Kill the Cancer
604   Cell! *Clin Cancer Res* **21**:5015–5020. doi:10.1158/1078-0432.CCR-15-1204

605 Liao PC, Tandarich LC, Hollenbeck PJ. 2017. ROS regulation of axonal
606   mitochondrial transport is mediated by Ca2+ and JNK in Drosophila. *PLoS*
607   *One* **12**:1–21. doi:10.1371/journal.pone.0178105

608 Li L, Nørrelkke SF, Cox EC. 2008. Persistent cell motion in the absence of
609   external signals: A search strategy for eukaryotic cells. *PLoS One* **3**.
610   doi:10.1371/journal.pone.0002093

611 Li-Shishido S, Watanabe TM, Tada H, Higuchi H, Ohuchi N. 2006. Reduction in
612   nonfluorescence state of quantum dots on an immunofluorescence staining.
613   *Biochem Biophys Res Commun* **351**:7–13. doi:10.1016/j.bbrc.2006.09.159

614 Ma Y, Guo S, Pan Y, Fan R, Smith ZJ, Lane S, Chu K. 2019. Quantitative phase
615   microscopy with enhanced contrast and improved resolution through
616   ultra-oblique illumination (UO-QPM). *J Biophotonics* 1–13.
617   doi:10.1002/jbio.201900011

618 Maddah M, Heidmann JD, Mandegar MA, Walker CD, Bolouki S, Conklin BR,
619   Loewke KE. 2015. A non-invasive platform for functional characterization of
620   stem-cell-derived cardiomyocytes with applications in cardiotoxicity testing.
621   *Stem Cell Reports* **4**:621–631. doi:10.1016/j.stemcr.2015.02.007

622 Maharana S, Munder MC, Ulbricht E, Otto O, Müller P, Franzmann T,
623   Taubenberger A, Nüske E, Malinovska L, Herbig M, Midtvedt D, Guck J,
624   Alberti S, Zaburdaev V, Richter D. 2016. A pH-driven transition of the
625   cytoplasm from a fluid- to a solid-like state promotes entry into dormancy.
626   *Elife* **5**:1–30. doi:10.7554/elife.09347

627 Martindale JL, Holbrook NJ. 2002. Cellular response to oxidative stress:
628   Signaling for suicide and survival. *J Cell Physiol* **192**:1–15.
629   doi:10.1002/jcp.10119

630 Masuzzo P, Van Troys M, Ampe C, Martens L. 2016. Taking Aim at Moving
631   Targets in Computational Cell Migration. *Trends Cell Biol* **26**:88–110.
632   doi:10.1016/j.tcb.2015.09.003

633 Mitsunaga M, Ogawa M, Kosaka N, Rosenblum LT, Choyke PL, Kobayashi H.
634   2011. Cancer cell–selective in vivo near infrared photoimmunotherapy
635   targeting specific membrane molecules. *Nat Med* **17**:1685–1691.
636   doi:10.1038/nm.2554

637 Murphy MP. 2013. Mitochondrial dysfunction indirectly elevates ROS production
638   by the endoplasmic reticulum. *Cell Metab* **18**:145–146.
639   doi:10.1016/j.cmet.2013.07.006

640 Nagaya T, Nakamura Y, Sato K, Harada T, Choyke PL, Kobayashi H. 2016.
641   Near infrared photoimmunotherapy of B-cell lymphoma. *Mol Oncol*
642   **10**:1404–1414. doi:10.1016/j.molonc.2016.07.010

643 Redza-Dutordoir M, Averill-Bates DA. 2016. Activation of apoptosis signalling
644   pathways by reactive oxygen species. *Biochim Biophys Acta - Mol Cell Res*
645   **1863**:2977–2992. doi:10.1016/j.bbamcr.2016.09.012

646 Sakuma M, Kita S, Higuchi H. 2016. Quantitative evaluation of malignant
647   gliomas damage induced by photoactivation of IR700 dye Publisher : Taylor
648   & Francis **6996**. doi:10.1080/14686996.2016.1205936

649 Shi H, Kwok RTK, Liu J, Xing B, Tang BZ, Liu B. 2012. Real-time monitoring of
650   cell apoptosis and drug screening using fluorescent light-up probe with
651   aggregation-induced emission characteristics. *J Am Chem Soc* **134**:17972–
652   17981. doi:10.1021/ja3064588

653 Tada H, Higuchi H, Wanatabe TM, Ohuchi N. 2007. In vivo real-time tracking of
654   single quantum dots conjugated with monoclonal anti-HER2 antibody in
655   tumors of mice. *Cancer Res* **67**:1138–1144.
656   doi:10.1158/0008-5472.CAN-06-1185

657 Tokumitsu A, Wakitani S, Takagi M. 2010. Noninvasive discrimination of human
658 normal cells and malignant tumor cells by phase-shifting laser microscopy. *J*
659 *Biosci Bioeng* **109**:499–503. doi:10.1016/j.jbiosc.2009.10.020

660 Waters JC. 2009. Accuracy and precision in quantitative fluorescence
661 microscopy. *J Cell Biol* **185**:1135–1148. doi:10.1083/jcb.200903097

662 Yamaguchi Y, Shinotsuka N, Nonomura K, Takemoto K, Kuida K, Yosida H,
663 Miura M. 2011. Live imaging of apoptosis in a novel transgenic mouse
664 highlights its role in neural tube closure. *J Cell Biol* **195**:1047–1060.
665 doi:10.1083/jcb.201104057

666 Yildiz A, Selvin PR. 2005. Fluorescence imaging with one nanometer accuracy:
667 Application to molecular motors. *Acc Chem Res* **38**:574–582.
668 doi:10.1021/ar040136s

669 Zhang G, Gurtu V, Kain SR, Yan G. 1997. Annexin V-FITC Binding Assay.
670 *Biotechniques* **25**:525–531. doi:10.2144/97233pf01

671 Zhang Y, Tewson PH, Ding Y, Li J, Enterina JR, Quinn AM, Maysinger D, Mo
672 GCH, Zhang J, Shen Y, Alford SC, Campbell RE, Zhang I, Hughes TE. 2015.
673 Ratiometric biosensors based on dimerization-dependent fluorescent
674 protein exchange. *Nat Methods* **12**:195–198. doi:10.1038/nmeth.3261